International Journal of Multiphase Flow 35 (2009) 288–296

Contents lists available at ScienceDirect

International Journal of Multiphase Flow

journal homepage: www.elsevier.com/locate/ijmulflow

The influences of jet precession on near field particle distributions

C.H. Birzer *, P.A.M. Kalt, G.J. Nathan

University of Adelaide, School of Mechanical Engineering, Adelaide SA 5005, Australia

ARTICLE INFO

Article history:
Received 17 June 2008
Received in revised form 27 October 2008
Accepted 31 October 2008
Available online 24 November 2008

ABSTRACT

The effects of jet precession on the mean and fluctuating components of the distributions of 20 μm spherical particles in the first 10 nozzle diameters downstream from a simulated pulverised fuel burner have been investigated experimentally. Precessing jets are a class of oscillating flow with application in the combustion of pulverised fuels, especially in rotary kilns. The particle distributions have been determined using *planar nephelometry*, a laser-based instantaneous concentration technique. The influence of the momentum ratio of precessing jet to co-annular jet flow on the distribution of particles is assessed. Mean and fluctuating components of centreline particle distributions, half-widths and radial profiles are presented. It is found that small amounts of jet precession result in an elongation and narrowing of the overall particle distributions. Further increases of precessing jet momentum leads to a wider distribution of particles.

1. Introduction

Precessing jet (PJ) flows have been studied over the last couple of decades because of the beneficial influences on mixing they offer in some applications (Nathan and Luxton, 1992; Schneier et al., 1997; Smith et al., 1998b; Wong et al., 2003). The PJ nozzle consists of a large sudden expansion, chamber, and small lip. Fluid enters the chamber via the sudden expansion. If the inlet flow Reynolds number is sufficiently large, $Re_{inlet} \gtrsim 20{,}000$, the dominant flow mode comprises an asymmetrically reattaching flow that precesses naturally about the nozzle axis, due to a naturally occurring flow instability (Nathan et al., 1998). The flow emerges from the nozzle without filling the entire exit plane, and continues to precess in the near external field (Wong et al., 2003). Due to the small lip at the exit plane, the flow exits at a deflection angle of about 45° to the nozzle axis. The unsteady flow results in a rapid initial jet spread, where the initial entrainment of ambient fluid is enhanced by up to a factor of 5 relative to a simple jet (Nathan, 1988). However, entrainment is restricted within the nozzle chamber and the far-field rates of spread and decay are comparable with that of a simple jet (Nathan et al., 2006). A schematic diagram of a PJ with co-annular nozzle is shown in Fig. 1. The details of the configuration are discussed in Section 2.4.

PJ flows can be beneficial in natural gas-fired rotary cement kilns, as they can provide a 40–60% reduction in NO_X emissions (Nathan and Manias, 1995), while also improving product quality and fuel savings by typically 4–8%. Product quality is increased by maximising the clinker cooling rate (Ono, 1980). Here, an increased clinker cooling rate is achieved by translating the peak release closer to the burner. The full-scale measurements of Nathan and Manias (1995) are consistent with the pilot-scale measurements of Parham et al. (2000). They measured a 4% increase in radiant heat transfer and inferred a 30% reduction in NO_X emissions relative to a high momentum jet flame with a Craya–Curtet number of 2.7. The results are also consistent with trends in laboratory scale flames, which show that the initial radial spread leads to decreased global mixing rates, increased presence of soot, increased radiation and decreased thermal NO_X emissions Nathan et al. (2006).

In the cement industry, approximately 90% of rotary kilns use pulverised fuel (PF) such as pulverised coal. There is less information available on the influence of PJ flows on two-phase flows and flames than in gas flames. Nevertheless, the PJ nozzle has also shown benefits in pulverised coal fired rotary cement kilns (Megalos et al., 2001; Smith et al., 2002). Smith et al. (1998a) reported that, for PF flames, the PJ nozzle aerodynamics can reduce flame standoff (i.e. ignition distances) by a factor of 4, resulting in improved flame stability and lower fuel NO_X emissions. These features correlate with the enhanced formation of high localised particle concentrations, known as particle clusters, particularly in the near burner regions (Smith et al.,1998a, 2002). Nathan and Hill (2001, 2002) showed that the PJ provided a 3–5% reduction in NO_X and a 5% increase in fuel efficiency in a short-term trial at Ash Grove Cement. However, the complex interaction between particles and the fluid remains poorly understood. No detailed measurements of the influence of jet precession on the instantaneous particle distributions have been reported in the literature.

The addition of a solid-phase can have a significant influence on the flow (Di Giancinto et al., 1982). Two-phase flows typically exhibit lower velocity decay rates of transport fluid (Fleckhaus et al., 1987). Sheun et al. (1985) reported that increasing the particle

* Corresponding author. Tel.: +61 8 8303 3157; fax: +61 8 8303 4367.
E-mail address: cristian.birzer@adelaide.edu.au (C.H. Birzer).

0301-9322/$ - see front matter © 2009 Published by Elsevier Ltd.
doi:10.1016/j.ijmultiphaseflow.2008.10.009

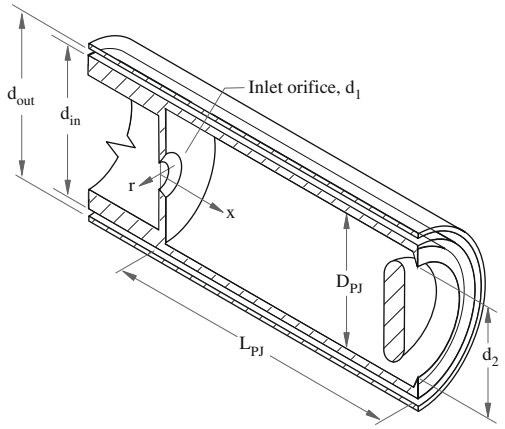

Fig. 1. A schematic diagram of the co-annular nozzle.

mass loading reduces the velocity decay rate of both phases. The solid-phase is an additional source of momentum and the transfer of momentum between the phases is coupled with the particle dispersion. Crowe et al. (1985) showed that particle dispersion is controlled by the Stokes number, *Sk*, which is the ratio of particle response time, τ_p, to fluid time scale, τ_f. Particles of $Sk \ll 1$ respond to both large and smaller eddies, and therefore closely follow the motions of the surrounding fluid. Particles with $Sk \gg 1$ have substantially higher momentum and do not respond significantly to any fluid motions. Particles with $Sk \approx 1$ exhibit a partial response to the flow (Longmire and Eaton, 1992). For particle Reynolds number less than 0.1 the particle response time is typically calculated by

$$\tau_p = \frac{\rho_p d_p^2}{18\mu}, \tag{1}$$

where d_p is the particle diameter, ρ_p is the particle density and μ is the kinematic viscosity. The large-eddy fluid time scale is characterised by $\tau_f = \frac{L}{U}$, where L is the characteristic length scale of the flow and U is the characteristic fluid velocity. The Stokes number for creeping flows is therefore commonly represented as

$$Sk = \frac{\rho_p U d_p^2}{18\mu L}. \tag{2}$$

However, a wide range of alternative definitions for L and U have been used, dependent upon the applications (Longmire and Eaton, 1990, 1992; Aggarwal, 1993; DeSpirito and Wang, 2001; Uchiyama and Fukase, 2006).

Smith et al. (1998a,b) and Nathan et al. (2000) characterised L for the flow from a precessing jet nozzle to be $L = 3D_{PJ}$ (see Fig. 1) as it corresponds well with the scale of the large structures observed visually in the near nozzle region of the nozzle. They also characterised U by the momentum weighted mean, U_{total} of the total velocities of the different streams

$$U_{total} = \frac{U_{cen}G_{cen} + U_{ANN}G_{ANN} + U_{co}G_{co}}{G_{cen} + G_{ANN} + G_{co}}, \tag{3}$$

where U and G are velocity and momentum flux, respectively. The subscripts cen, ANN, and co represent the central, annular and co-flows. These definitions are followed in the present work.

While *Sk* is defined for a single particle in suspension, it has been successfully extended to multiple particles. This requires the assumption that particle–particle interactions are negligible, and hence the volume fraction of particles is below 0.3%. This is the case for many experimental and industrial cases (Batchelor (1971) quoted by Hardalupas et al. (1989)).

The distribution of particles also depend on the particle mass loading (Di Giancinto et al., 1982; Fan et al., 1992). The mass loading ratio, β, is defined by Di Giancinto et al. (1982) to be the ratio of solid-phase mass to gaseous-phase mass per unit volume of suspension. For the current work, β is defined as the ratio of solid-phase mass flow rate to the conveying air mass flow rate

$$\beta = \frac{\dot{m}_p}{\dot{m}_{f_{ANN}}}. \tag{4}$$

Here f_{ANN} designates the annular conveying fluid. For the current work particle and conveying flow rates are constant, so that $\beta = 0.14 \pm 0.02$.

Due to the erosive nature of conveyed solid particles, the solid-phase in the burner configuration, used previously by Smith et al. (1998a) and in the present study, was conveyed via a co-annular nozzle (Fig. 1). The central PJ flow is utilised to modify the particle distributions and will, in turn, be modified by the particles. The momentum of the PJ relative to the momentum of the particle-laden annular jet has been shown to characterise distribution of particles and the performance of a burner to first order (Smith et al., 1998a,b). The momentum flux, G, (in Newtons) of a two-phase stream is

$$G = G_f + G_p = \frac{\dot{m}_f}{A\rho_f} + \frac{\dot{m}_p}{A\rho_p}, \tag{5}$$

where $\dot{m}$ is the mass flow rate, ρ is the fluid density, A is the cross-sectional area and subscripts f and p designate fluid and particles, respectively.

The emerging PJ flow does not fill the entire exit plane of the PJ nozzle, but occupies approximately one third of the exit plane (Wong et al., 2003). Accordingly, the exit momentum flux of a PJ may be estimated to be

$$G_{PJ} = \frac{12\dot{m}_{PJ}^2}{\pi\rho(D_{PJ}^2 - 0.79D_{PJ}^2)}. \tag{6}$$

The aim of the present investigation is to determine the influence of the momentum ratio of PJ to annular jet streams, G_{PJ}/G_{ANN}, on the mean and fluctuating components of the distribution of particles. The aim is also to increase understanding of two-phase jet flows. The work is motivated by a desire to support further optimisation of burner designs in PF-fired rotary kilns.

2. Equipment and methodology

2.1. Wind tunnel

Experiments were conducted in an open loop wind tunnel to simulate the near-nozzle region of a pulverised-coal burner. The experiments were non-reacting and conducted at room-temperature, since it is necessary to understand the non-reacting flow before proceeding to a reacting case. However, the data are also directly relevant to the near-nozzle, pre-ignition region of a PF flame, where thermal gradients are small relative to the combustion zones (Smart, 1992).

The wind tunnel is vertically oriented to avoid gravity bias and has a square cross-section of 650 mm × 650 mm and a working section of 1500 mm length. The tunnel has a constant co-flow of 8.0 ± 0.3 m/s, which is typical of the velocity in a rotary cement kiln. This flow is conditioned by a series of wire-mesh screens and a honeycomb section upstream from the working section. Directly downstream from the working section is another wire-mesh screen. Further downstream is a cyclone separator is used to remove particulate matter from the exhaust air. The walls of the working section are constructed from 16 mm thick Perspex enabling the application of laser-based measurement techniques.

2.2. Laser diagnostics

The laser-based technique used to measure particle distributions was *Planar Nephelometry*. This technique infers the particle distribution from the recorded Mie scattering. For planar nephelometry, attenuation of in-plane light was corrected using algorithms provided by Kalt et al. (2007) and Kalt and Nathan (2007). For the current work the estimated uncertainty of the applied corrections is 3%.

At the same time, the particle number density cannot be determined without the additional assumption that size distribution is consistent throughout the flow. For this reason, all data are presented in terms of surface area, which does not require this assumption to be made. Nevertheless, since $Sk \leqslant 0.5$ for all particles and the average $Sk \approx 0.08$ (see Section 2.5), all particles respond well to the dominant large-scale motions. On this basis, while some variations in size distribution through the flow are inevitable, they are expected to be small, and the term "apparent concentration" is also employed in the text.

2.3. Laser optics

A Nd:YAG laser, frequency doubled to 532 nm, was used to illuminate the viewing plane, which measured approximately 530 mm × 525 mm. A series of optics were used to create a light sheet less than 2 mm thick through the central plane of the jet. The light scattered from particles (discussed in Section 2.5) were recorded on a Kodak Megaplus CCD of 1018 × 1008 pixels with 10-bit resolution, synchronised with the laser. This results in a resolution of approximately 520 μm × 520 μm × 2000 μm per pixel. A main advantage of the technique is that it does not require individual particles to be identified; therefore the volume imaged by each pixel can be much greater than that of individual particle. The CCD had a polarised filter attached, orientated to collect light in the same polarisation as the light sheet (i.e. horizontally). This filter was used to reduce the signal from multiple scatterings out-of-plane which depolarise the scattered light. For each experimental case, some 200 Mie-scattering images were recorded. A schematic diagram of the experimental arrangement in shown in Fig. 2.

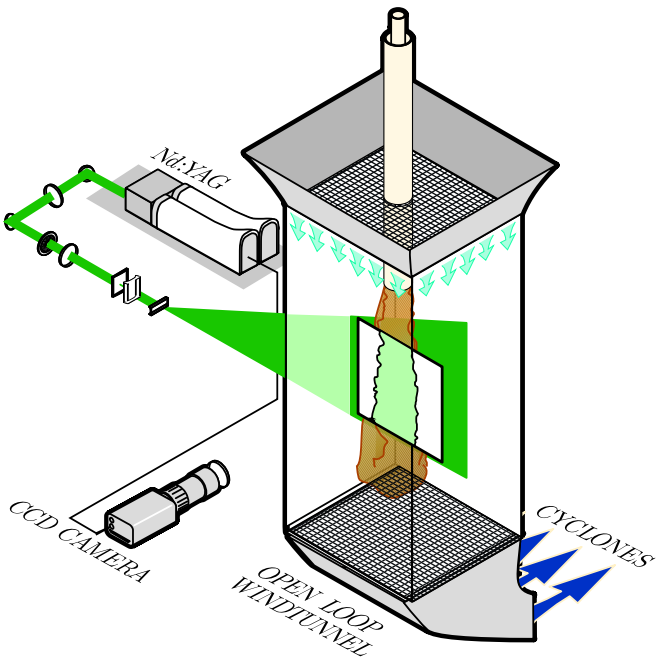

Fig. 2. A schematic diagram of the experimental apparatus.

2.4. Nozzle

The nozzle consisted of a central precessing jet nozzle, within a co-annular nozzle, as shown schematically in Fig. 1. Upstream from the PJ chamber is a 1500 mm long, 50 mm internal diameter pipe. This feeds a smooth contraction to a 10 mm diameter inlet, d_1, into the PJ chamber. The PJ chamber has an internal diameter, D_{PJ}, of 50 mm and length, L_{PJ}, of 140 mm. A 45° contraction at the end of the PJ chamber results in an exit diameter, d_2, of 40 mm. The dimensions were selected based on the recommendations of Wong et al. (2003). The annular nozzle has inner and outer diameters of 60 mm and 70 mm, respectively, and total length of 1700 mm, which equates to over 340 gap diameters. The annular gap was consistently 5 mm, with care taken to minimise asymmetry.

2.5. Solid phase

Pulverised-coal particles were simulated using hollow glass spheres (Q-Cel™ 5070s). These particles have a specified density, ρ_p, of 700 kg/m^3, which is about half that of coal. Fig. 3(a) shows the particles under magnification. A Malvern particle sizer was used to measure volume-weighted distribution of particle diameters, $d_{3,2}$. The signal from Lorenz–Mie scattering is proportional to the surface area of scattering bodies, A_p. The distribution results provided by the Malvern particle sizers are converted to surface area weighted distributions to maintain consistency with Planar Nephelometry. The surface area is also of direct relevance to combustion reaction rates, since reaction occur at the surface.

The PDFs of particle diameter distributions based on the percentage of both particle volume, $d_{3,2}$, and particle surface area, $d_{2,1}$, are shown in Fig. 3(b). It is evident that 85% of particles, by surface area, have a diameter in the range of $7 \leqslant d_{2,1} \leqslant 50$ μm. This is broader than the manufacturer's specified range of 25–45 μm. The mean values of $d_{2,1}$ for the particles used in the current investigation was determined to be approximately 20 μm. Based on $d_{2,1}$, a length scale, $L = 3 \times D_{PJ}$, and U_{total}, the particles have a Stokes number of $Sk \leqslant 0.50$ and an average of $Sk \approx 0.08$. An alternative calculation for Sk can be determined using $\tau_f = 1/f_p$ where f_p is the frequency of precession (see Section 2.6). Using this alternate mean, the particles have $Sk \leqslant 0.2$. From both of these estimates, it is expected that most particles will follow the large-scale motions reasonably closely, but some departure may be evident with the largest particles. This allows the response of the particles to the near-field flow to be estimated. As a result, it is expected that most particles will follow the large-scale motions reasonably closely, but some departure may be evident with the largest particles. Despite the quite large particle size distribution, it is narrower than that of Fan et al. (1990), and only slightly wider than that of Ayranci et al. (2007). The range of particle sizes is also similar to that of Hardalupas and Horender (2003) and significantly narrower than that of Geiss et al. (2004), although the mean diameter is much smaller for the current work.

2.6. Flow parameters

Filtered and compressed air was supplied through both the annular and central jets. The velocity at the PJ inlet was varied between $0 \leqslant U_1 \leqslant 287$ m/s. This gives a Reynolds number range, based on d_1 (Fig. 1), of $Re_{PJ} \leqslant 188{,}500$. Based on Nathan et al. (1998), the frequency of precession, f_p, was estimated to be 7 Hz. The annular velocity $U_{ANN} = 18$ m/s was not varied. The Reynolds number based on the annular gap was $Re_{ANN} = 5900$. Details of the experimental conditions are summarised in Table 1.

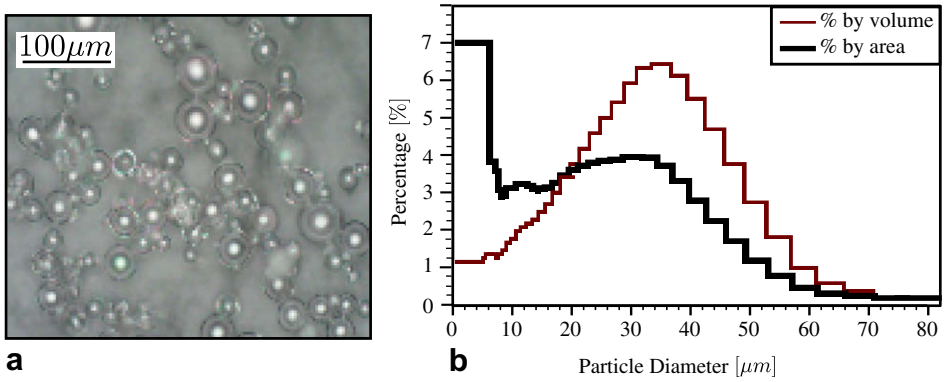

Fig. 3. (a) The 20 μm nominal diameter glass spheres used in the investigation under magnification. (b) The size distribution of the particles, as measured by a Malvern particle sizer.

Table 1
Operating conditions.

Parameter	Experimental run number						
	1	2	3	4	5	6	7
PJ inlet jet velocity, $U_{PJ(inlet)}$ [m/s]	0.0	22	54	99	154	211	286
PJ inlet Reynolds number, $Re_{PJ(inlet)}$	0.0	14,245	35,612	64,218	101,947	138,955	188,532
PJ momentum flux, G_{PJ} [N]	0.000	0.014	0.086	0.290	0.709	1.32	2.42
Annular jet velocity, U_{ANN} [m/s]	18.0	18.0	18.0	18.0	18.0	18.0	18.0
Annular Reynolds number, Re_{ANN}	5935	5935	5935	5935	5935	5935	5935
Annular momentum flux, $G_{ANN(f)}$ [N]	0.39	0.39	0.39	0.39	0.39	0.39	0.39
Annular momentum flux, G_{ANN} [N]	0.47	0.48	0.49	0.50	0.51	0.51	0.49
Momentum ratio, G_{PJ}/G_{ANN}	0.00	0.03	0.18	0.58	1.46	2.60	4.90
Momentum ratio, $G_{PJ}/G_{ANN(f)}$	0.00	0.04	0.22	0.74	1.81	3.36	6.19
Particle mass loading ratio, β	0.120	0.129	0.148	0.152	0.158	0.161	0.148

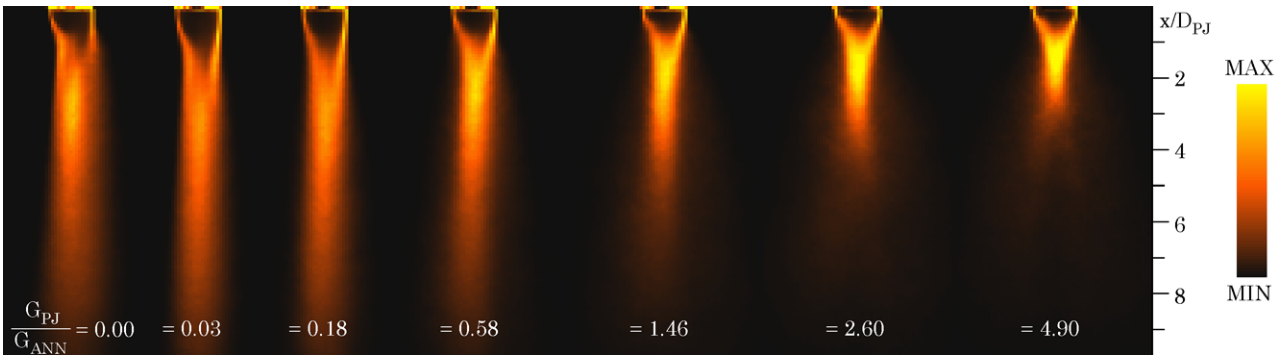

Fig. 4. Mean particle distributions for $0.00 \leqslant G_{PJ}/G_{ANN} \leqslant 4.90$. Images are normalised to the maximum signal in each image.

3. Results and discussion

3.1. Influence of momentum ratio on the mean particle distribution

Fig. 4 shows the normalised mean particle distributions for seven cases of momentum ratios ranging from $0.00 \leqslant G_{PJ}/G_{ANN} \leqslant 4.90$. For each image, separate scaling of the false colour[1] map is used for clarity. The fluid-phase momentum flux of the annulus, $G_{ANN(f)}$, β, and therefore G_{ANN} are held constant in all cases. A qualitative trend of significantly increasing spread and decay rates with increasing G_{PJ}/G_{ANN} can be seen.

It can be seen that the initial particle distributions immediately downstream from the jet exit are not symmetrical about the nozzle

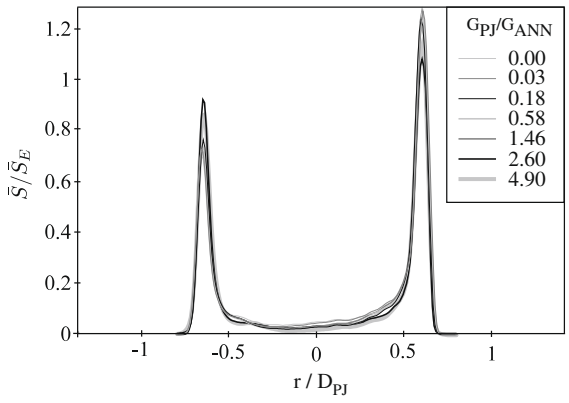

Fig. 5. Radial profiles of normalised mean signals at $x/D_{PJ} = 0.1$ indicating bias due to asymmetry in the annulus.

[1] For interpretation of the references to colour in Fig. 4, the reader is referred to the web version of this paper.

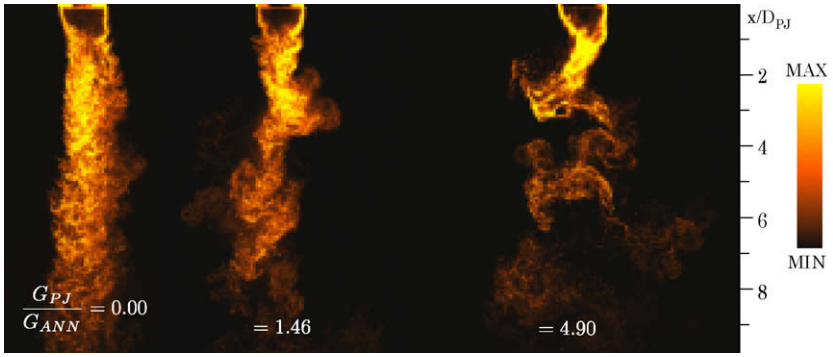

Fig. 6. Instantaneous images for G_{PJ}/G_{ANN} = 0.00, 1.46 and 4.90.

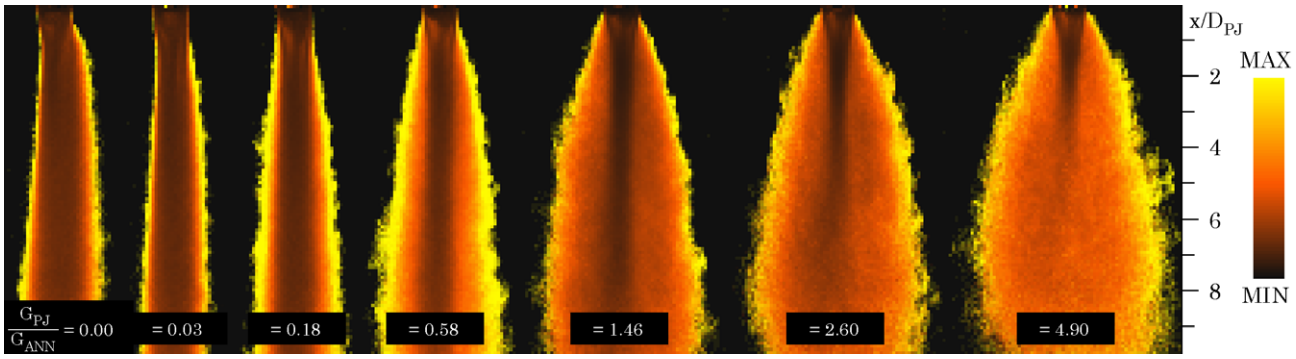

Fig. 7. A set of images of the relative fluctuations, $S'/\overline{S}$, for $0.00 \leqslant G_{PJ}/G_{ANN} \leqslant 4.90$. The false colour map is optimised for each case. (For interpretation of the references to colour in this figure legend, the reader is referred to the web version of this paper.)

axis. This asymmetry is due to a non-uniform azimuthal distribution of particles in the co-annular jet, possibly due to a roping phenomenon within the co-annulus. The bias is particularly evident for G_{PJ}/G_{ANN} = 0.00 and can be seen to persist downstream. However, increasing G_{PJ}/G_{ANN} reduces the influence of the asymmetry.

The particle distributions at the exit plane cannot be measured accurately due to interference of light scattered by the nozzle. However, this interference is negligible for $x/D_{PJ} \geqslant 0.1$. Therefore this location is used as the closest practical measure of distributions in the nozzle exit plane. The radial profiles at x/D_{PJ} = 0.1 are presented in Fig. 5. The profiles are normalised by the average of the maximum signal from each side of the annulus, along this radius for each case, which is termed $\overline{S}_E$.

The normalised particle distributions at x/D_{PJ} = 0.1 clearly show significant particle bias with an asymmetry about the nozzle axis. This bias results in a difference in mean signal strength of approximately 33 ± 3% for all cases except for the highest momentum ratio case, G_{PJ}/G_{ANN} = 4.90, where the bias is 20%. This indicates that the influence of the PJ for high G_{PJ}/G_{ANN} is significant upstream from x/D_{PJ} = 0.1.

Fig. 6 provides three instantaneous images. These images correspond to the mean images shown in Fig. 4 for G_{PJ}/G_{ANN} = 0.00, 1.46 and 4.90. By comparison of Fig. 4 to Fig. 6 it can be seen that, for G_{PJ}/G_{ANN} = 0.00, the shape of the instantaneous distribution of particles is similar to that of the mean. However, the instantaneous images become increasingly different from the mean with increased G_{PJ}/G_{ANN}. These images also confirm that the particles exhibit a strong response to the dominant large-scale flow oscillations.

The relative intensity of the fluctuating component of the particle distribution is determined by normalising the standard deviation of the particle distribution, S', by the local mean particle distribution, $\overline{S}$. This is termed the *relative fluctuations*. The relative fluctuations of the seven different momentum ratio cases are shown in Fig. 7. The scale of the false colour[2] map is set to highlight features in each case, and so differ from case to case. In particular, these images highlight the edges of the jets since, unlike the mean, the relative fluctuations exhibit very steep gradients near the jet edge. In support of the findings from the mean data, the particle bias of the emerging jet is evident for G_{PJ}/G_{ANN} = 0.00 and 0.03. However, the influence of particle bias is less pronounced for $G_{PJ}/G_{ANN} \geqslant 0.18$. The bias is not clearly noticeable at the nozzle exit plane for G_{PJ}/G_{ANN} = 4.90.

Increasing G_{PJ}/G_{ANN} above 0.18 results in increased spread of the jet edge. Interestingly, this figure also shows that the spreading angle of the PJ flows decrease with axial distance. That is, the spreading rate is greatest close to the nozzle and decreases towards the downstream end of the image. This is consistent with trends in single-phase investigations, where the PJ flow is found to converge toward a far-field state comparable with a simple jet (Nathan et al., 2006). The jet spread is also comparable with that in particle-laden swirling, coaxial jets with forced vortex generators investigated by Wicker and Eaton (1999).

Fig. 8 shows the mean distributions of particle along the nozzle axis for the cases shown in Fig. 4. For each case, the mean signal, $\overline{S}$, is normalised by the peak mean signal along the centreline, $\overline{S}_P$. It can be seen that there is an initial increase in $\overline{S}/\overline{S}_P$ to a peak associated with the convergence of the co-annular stream towards the centreline. The distance from the nozzle exit plane to this peak is termed x_p.

[2] For interpretation of the references to colour in Figs. 6, 7 legend, the reader is referred to the web version of this paper.

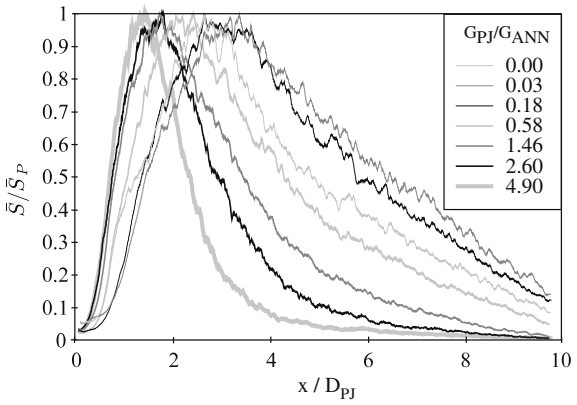

Fig. 8. Normalised axial mean particle distributions along the nozzle axis for varying values of G_{PJ}/G_{ANN}.

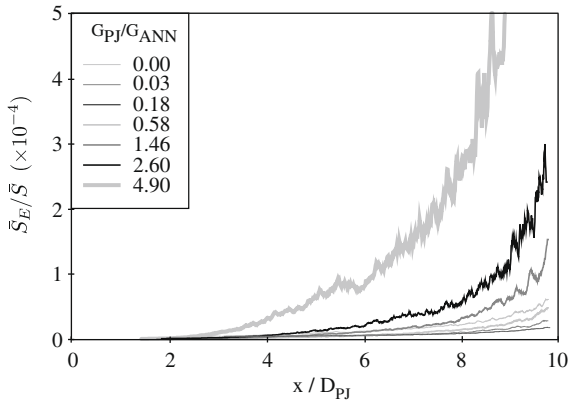

Fig. 10. Inverse axial mean particle distributions along the nozzle axis for varying values of G_{PJ}/G_{ANN} and $x/D_{PJ} \geqslant x_p$.

An increase from $G_{PJ}/G_{ANN} = 0.00$ to $G_{PJ}/G_{ANN} = 0.03$ causes a decrease in the initial concentration gradient through this convergence region. Subsequent increases in G_{PJ}/G_{ANN} cause this gradient to increase. It is only when $G_{PJ}/G_{ANN} \geqslant 0.58$ that the initial rate of increase in apparent particle concentration is greater than that for $G_{PJ}/G_{ANN} = 0.00$. Downstream from x_p, the decay in centreline concentration can be seen to be highly dependent on G_{PJ}/G_{ANN}. Fig. 9 illustrates these divergence and convergence regions in relation to x_p.

Fig. 10 presents inverse normalised axial mean particle distributions, $\bar{S}_E/\bar{S}$, for $x/D_{PJ} \geqslant x_p$. These profiles highlight the influence of jet precession on the centreline decay rate over the region $4 \leqslant x/D_{PJ} < 10$, and so complements Fig. 8. From these results it is clear that for $G_{PJ}/G_{ANN} \leqslant 0.58$ there are only small difference between these profiles, but significant changes occur for $G_{PJ}/G_{ANN} \geqslant 0.146$. The profiles for $G_{PJ}/G_{ANN} < 1.46$ are not well resolved on this scale, but it is evident that they have not converged to a linear inverse decay within this axial range. Clearly, the profile for $G_{PJ}/G_{ANN} = 4.90$ exhibits a much higher decay rate than the other cases over the entire range downstream from x_p, and there is no evidence of the decay rate returning to a value more like that of a simple jet within this measurement range.

The dependence of both the location of x_p, and its magnitude, $\bar{S}_p$, on G_{PJ}/G_{ANN} are shown in Fig. 11 (note the two scales). The error bars correspond to a ±3% variation in the magnitude of the signal, $\bar{S}_p$. The influence of increased G_{PJ}/G_{ANN} is clearly evident and highlighted by the trend lines. An increase in G_{PJ}/G_{ANN} from 0.00 to 0.03

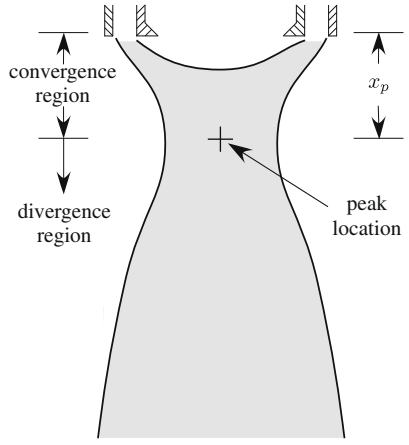

Fig. 9. Schematic diagram of the jet flow, showing the location of x_p and the convergence and divergence regions.

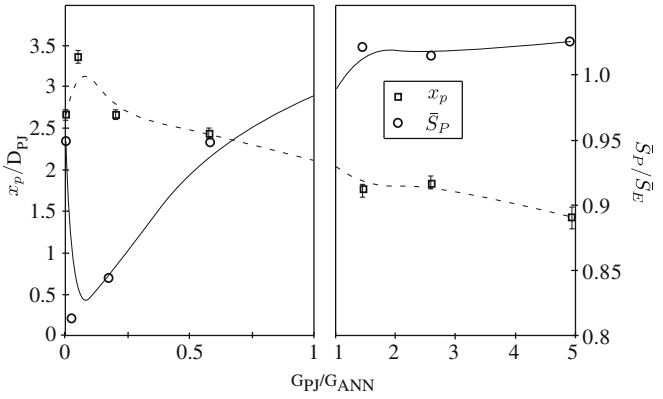

Fig. 11. Locations of x_p and normalised peak signal for varying G_{PJ}/G_{ANN}.

results in x_p being translated further from the nozzle exit. Subsequent increases in G_{PJ}/G_{ANN} translates x_p closer to the nozzle exit plane. Again, for the cases investigated, it is only for $G_{PJ}/G_{ANN} \geqslant 0.58$ that x_p is closer to the nozzle than for $G_{PJ}/G_{ANN} = 0.00$. A similar trend, but in the opposite direction, is exhibited by $\bar{S}_p$. The asymptotic-like convergence suggests that most of the benefits of jet precession can be expected to be achieved with $G_{PJ}/G_{ANN} \approx 4.90$, although some benefits are present as early as $G_{PJ}/G_{ANN} = 1.46$. The implication of these results is that the nozzle exhibits two possible modes; an axial-dominated mode, and a PJ-dominated mode. The axial-dominated mode occurs for $G_{PJ}/G_{ANN} < 0.18$ ($G_{PJ}/G_{ANN(f)} < 0.22$). The PJ-dominated mode occurs for $G_{PJ}/G_{ANN} \gtrsim 1.46$ ($G_{PJ}/G_{ANN(f)} \gtrsim 1.86$). For $0.18 \lesssim G_{PJ}/G_{ANN} \lesssim 1.46$ ($0.22 \lesssim G_{PJ}/G_{ANN(f)} \lesssim 1.86$) there is a transition between the two modes.

The corresponding radial profiles at their respective x_p are presented in Fig. 12. These values are normalised to $\bar{S}_P$. Although some asymmetry is present, the severity of asymmetries present at $x/D_{PJ} = 0.1$ (Fig. 5) are greatly reduced. All radial profiles shown in Fig. 12 exhibit approximately Gaussian distributions. The profiles on the left-hand side of the nozzle axis overlap more strongly than on the right-hand side. The location of the peaks is biased slightly towards the right-hand side of the nozzle axis; that is, to the side with the higher particle mass loading at the nozzle exit plane. Despite the bias, it is clear that G_{PJ}/G_{ANN} has a significant influence in reducing the profile widths at x_p. However, care must be taken in any direct comparison due to the different axial location of each profile. As the location of x_p corresponds approximately to the narrowest region of the jet, these results indicate that jet precession can cause a significant reduction in the minimum width of the jet.

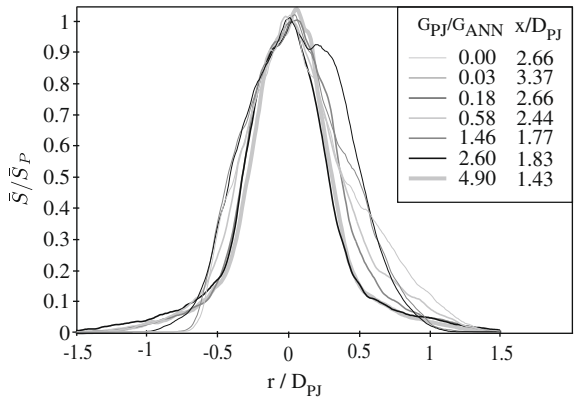

Fig. 12. Radial profiles of normalised mean signals at the axial location corresponding to their peak signals, x_p.

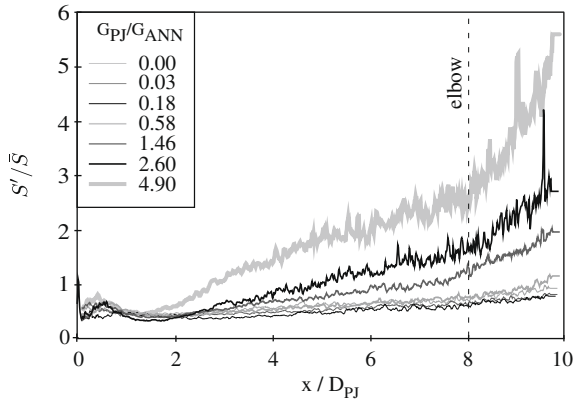

Fig. 13. Relative fluctuations of the centreline particle distributions.

The relative fluctuations along the centreline are shown in Fig. 13. For $G_{PJ}/G_{ANN} \geqslant 0.58$ a near-field hump in $S'/\bar{S}$ is found at $x/D_{PJ} \approx 0.5$. This near-field hump is not evident for the cases with lower G_{PJ}. Further downstream in the region of $1.4 \lesssim x/D_{PJ} \lesssim 3.4$, each case exhibits a local minimum. These minima correspond to the respective locations of x_p. This is because the instantaneous jet cuts across the nozzle axis at x_p, drawing particles with it. Hence, the precession always takes the particles through this point, so that the relative fluctuations are lowest. (Note that the cycle to cycle variations are still significant.) Downstream from x_p, $S'/\bar{S}$ steadily increases for all cases. This increase is marginally steeper

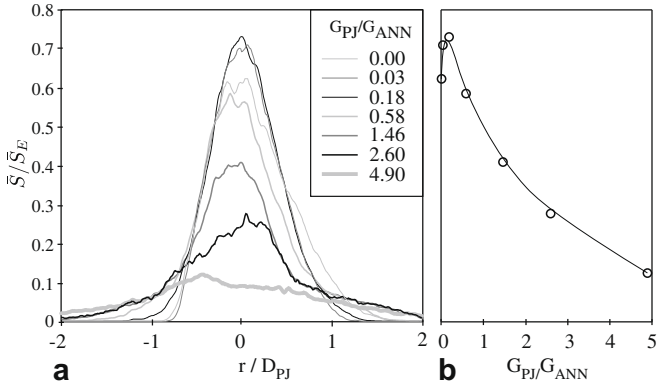

Fig. 14. Radial profiles of normalised mean signals at the $x/D_{PJ} = 4$.

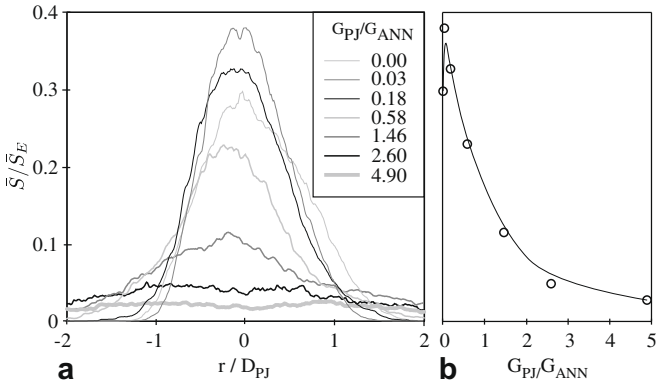

Fig. 15. Radial profiles of normalised mean signals at the $x/D_{PJ} = 7$.

for higher values of G_{PJ}/G_{ANN} between 0.00 and 0.58. For $G_{PJ}/G_{ANN} \geqslant 1.46$ this rate becomes much greater with increasing G_{PJ}/G_{ANN}. The increase in slope with increasing G_{PJ}/G_{ANN} is a result of the increased spreading of the mean jet and corresponding lower mean signal along the centreline. The profiles also exhibit a sudden change in slope, or an elbow point, at $x/D_{PJ} \approx 8$.

The radial profiles at $x/D_{PJ} = 4$ and 7 are presented in Figs. 14 and 15, respectively. The profiles are normalised to $\bar{S}_E$ for each case, as before. The radial profiles show that the influence of particle bias is greatly reduced at these axial locations, but some evidence of the bias persists. A clear trend is apparent, that a small increase in G_{PJ}/G_{ANN} from zero results in a taller, narrower near-field peak. However, further increases for $G_{PJ}/G_{ANN} \geqslant 0.58$ result in a significant lowering and broadening of the peak. At $x/D_{PJ} = 4$ the profiles of $G_{PJ}/G_{ANN} = 0.03$ and 0.18 are similar, and exhibit little bias. The radial profiles for $G_{PJ}/G_{ANN} = 0.00$ and $G_{PJ}/G_{ANN} = 0.58$ are also similar.

Figs. 14 and 15 also show corresponding plots of the peak value of $\bar{S}_E$ with variations to G_{PJ}/G_{ANN}. These profiles highlight the strong similarities in the trends discussed.

The trend of flatter, wider profiles for increasing G_{PJ}/G_{ANN} in the range $G_{PJ}/G_{ANN} \geqslant 0.03$ is also evident at $x/D_{PJ} = 7$. A notable difference in the radial profiles at $x/D_{PJ} = 7$ relative to $x/D_{PJ} = 4$ is that there are some regular variations between the different data sets. For example the peak at $G_{PJ}/G_{ANN} = 0.00$ differs much more from that at $G_{PJ}/G_{ANN} = 0.58$; and similarly for those at $G_{PJ}/G_{ANN} = 0.03$ and $G_{PJ}/G_{ANN} = 0.18$. Also, $G_{PJ}/G_{ANN} = 4.90$ is almost flat for $-1.5 \leqslant r/D_{PJ} \leqslant 1.5$. This is evidence of the flow exhibiting a transition from the near field to reach a more fully developed region by $x/D_{PJ} = 7$.

The relative fluctuations along radial profiles $x/D_{PJ} = 4$ and 7 are shown in Figs. 16 and 17, respectively. In all cases, except $G_{PJ}/G_{ANN} = 4.90$, a minimum is found near to the nozzle axis, and the relative fluctuations increase with radial distance away from the nozzle axis. The case $G_{PJ}/G_{ANN} = 4.90$ exhibits a small local maximum on the axis at $x/D_{PJ} = 7$. This small local maximum is not found further downstream for any case. At this point, $\bar{S}$ is unusually low, while the trend in absolute fluctuations does not vary.

A small increase in G_{PJ}/G_{ANN} from 0.00 to 0.03 results in a narrowing of the radial profile of the relative fluctuations at both axial locations. As discussed above, this range of G_{PJ}/G_{ANN} corresponds to axial-dominated flows. As G_{PJ}/G_{ANN} increases above $G_{PJ}/G_{ANN} \geqslant 0.03$, the flow becomes more PJ-dominated and the profile of the relative fluctuations at both radial locations becomes wider and flatter.

From Figs. 13, 16 and 17 it can be seen that for each case the relative fluctuations increase downstream from x_p and radially outwards from the nozzle centreline. A small increase in G_{PJ}/G_{ANN}

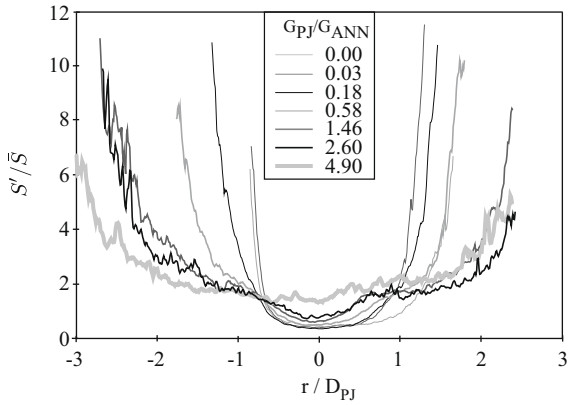

Fig. 16. Radial profiles of normalised relative fluctuations at $x/D_{PJ} = 4$.

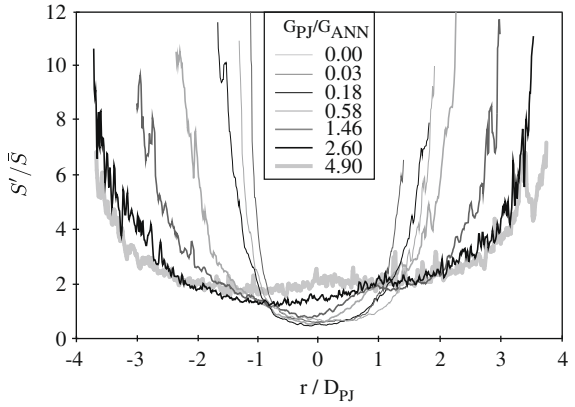

Fig. 17. Radial profiles of normalised relative fluctuations at $x/D_{PJ} = 7$.

from 0.00 to 0.03 results in a decrease in the relative fluctuations both axially and radially and a narrowing of the outer edge of the jets. However, further increases in $G_{PJ}/G_{ANN} \geqslant 0.18$ increases the fluctuations and the width of the outer edge of the jet downstream from x_p. This is due to the dominance of the PJ flow.

Fig. 18 shows the half-width concentration profiles for the seven cases. In all cases the half-widths initially converge to a narrow

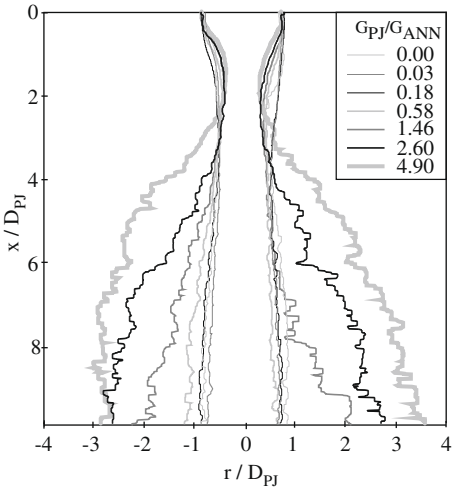

Fig. 18. Mean particle concentration half-width profiles.

waist and then diverge with increasing distance downstream. The waist for $G_{PJ}/G_{ANN} = 0.00$ is narrower than for $0.03 \leqslant G_{PJ}/G_{ANN} \leqslant 0.18$. For $G_{PJ}/G_{ANN} \geqslant 0.03$ an increase in G_{PJ}/G_{ANN} result in greater initial convergence rates and a narrowing of the waists. The divergence of the half-widths downstream from the waist are similar for cases $G_{PJ}/G_{ANN} \leqslant 0.58$. However, the divergence greatly increases with increases in $G_{PJ}/G_{ANN} \geqslant 1.46$.

From a comparison of Fig. 18 to Fig. 13 it can be seen that the elbow at $x/D_{PJ} \approx 8$ also corresponds to the location where the radial spread of the jet decreases. This is consistent with the trend shown in Fig. 14 where the peak in concentration is away from the centreline, suggesting a toroidal distribution.

It can also be seen from further reference to Figs. 16 and 17 that while increasing G_{PJ} for $G_{PJ}/G_{ANN} \geqslant 0.18$ results in a narrower waist as measured by the half-width. From the relative fluctuating data it can also be seen that this increase results in a wider spread of the absolute edge of the jet. This is also consistent with the particles responding well to the dominant large-scale oscillations. That is, the edge of the jet exhibits a different trend to the half-widths, in the necking region.

From these results it can be seen that jet precession has a very strong influence on mean and fluctuating component of the particle distributions. It is known that the instantaneous jet exiting from an unconfined PJ nozzle precesses about the nozzle axis with an initial deflection angle of approximately 45°. It also emerges from one side of the nozzle and crosses the nozzle axis. Increasing G_{PJ}, while all other variables remain constant, increases the local radial momentum of the total jet. It also increases the entrainment of ambient fluid and particles towards, and across, the nozzle axis. This explains the strong necking for the cases with high G_{PJ}/G_{ANN}. It also implies that the particles respond reasonably well to these large scale oscillations, as deduced from *Sk* being less than unity.

The case $G_{PJ}/G_{ANN} = 0.00$ corresponds to an annular jet. This configuration produces a central recirculation zone. With only a small flow through the central nozzle, the central PJ stream has insufficient momentum to have significant influence, but it does have sufficient flow to reduce, or even eliminate, the significance of the central recirculation zone. This explains why, in the mean distribution, a small increase in G_{PJ}/G_{ANN} from 0 to 0.03 results in a decrease in the initial convergence rates, pushes the location of x_p downstream, causes a widening of the waist, and decreases the rate of centreline and particle divergence.

For $G_{PJ}/G_{ANN} < 0.18$ the axial stream dominates the flow and distribution of particles. For $0.18 \lesssim G_{PJ}/G_{ANN} < 1.46$ there appears to be a transition from a axial-dominated flow to PJ-dominated flow. This is seen with a narrowing of the waists of the half-widths for increases in G_{PJ}/G_{ANN} above 0.18. Along the centreline, increasing G_{PJ} results in an increase in the initial particle convergence, a shift of x_p closer to the nozzle exit, and an increase in the rate of particle divergence downstream from x_p. The greater the value of G_{PJ}/G_{ANN}, the more pronounced these effects.

The flow for $G_{PJ}/G_{ANN} = 4.90$ has similarities to, and differences from, the swirling jet flows investigated by Wicker and Eaton (1999, 2001). As discussed earlier, the spread of the particles in these two flows is comparable. However, Wicker and Eaton (2001) found the recirculation zone in a particle-laden swirling jet to be devoid of particles. This axisymmetric zone is found slight downstream from the stagnation zone and can be easily identified by the bifurcation of the jet. In contrast, other single-phase investigations have shown that precessing-dominated flows do not generate a central recirculation zone (Wong et al., 2003). Likewise, there is no evidence of bifurcation in the particle distribution in the present flows, with the maximum concentration being found on the nozzle centreline.

4. Conclusions

Measurements have been performed of the influence of jet precession on the mean and fluctuating components of particle distributions in the near-field of a two-phase jet employing a precessing jet nozzle. The distribution of particles are found to be dominated by two separate modes; axial-, or PJ-dominated. The dominance of these modes depends on the relative momentum of the inner and outer streams. For $0.00 \leqslant G_{PJ}/G_{ANN} < 0.18$ the particle distributions are dominated by the influence of the axial stream. For $G_{PJ}/G_{ANN} \geqslant 0.58$ the distributions of particles are dominated by the PJ stream. A transition from axial to PJ dominance occurs for $0.18 \lesssim G_{PJ}/G_{ANN} < 1.46$.

The case $G_{PJ}/G_{ANN} = 0.00$ corresponds to an annular jet, which produces a central recirculation zone. Small increases in G_{PJ}/G_{ANN} while remaining in the regime that is classified as the axial-dominated mode, reduce, or even eliminate the significance of the central recirculation zone, causing an elongation of the overall jet. This results in x_p being translated further downstream, a widening of the waist, and a narrowing of the jet spread downstream from x_p.

For $G_{PJ}/G_{ANN} \geqslant 0.18$ the PJ flow dominates. Increases in G_{PJ}/G_{ANN} translate x_p closer to the nozzle exit plane, produce a narrower waist and increase the jet spread downstream from x_p. However, it is not until $G_{PJ}/G_{ANN} \geqslant 0.58$ that the PJ momentum is sufficient to have translated x_p closer to the nozzle than for $G_{PJ}/G_{ANN} = 0.00$. Similarly it is only when $G_{PJ}/G_{ANN} \geqslant 0.58$ that the spread of the jet downstream from x_p is greater and the waist is narrower than for $G_{PJ}/G_{ANN} = 0.00$. Increasing G_{PJ}/G_{ANN} above 0.58 also causes an increase in fluctuations relative to the mean This is consistent with the increased presence of clustering observed by Smith et al. (1998a, 2002). While the rate of spread has reduced by $x/D_{PJ} \approx 8$, the inverse centreline decay behaves differently, exhibiting increased inverse decay. This shows that the flow is still in transition to a far-field behaviour.

The particle bias emerging from the co-annulus will not propagate as strongly with sufficiently high G_{PJ}/G_{ANN}. A uniform particle distribution in an annular nozzle is unlikely in an industrial situation. Hence, the effect on performance of any initial particle bias is likely to be less significant when sufficient PJ flows are used to mitigate these effects.

Acknowledgments

The authors acknowledge the financial assistance provided to this project by the Australian Research Council through its Linkage Grant scheme and by industrial partner FCT-Combustion. The authors also acknowledge the reviewers for their helpful comments that have strengthened the paper considerably.

References

Aggarwal, S.K., 1993. Relationship between Stokes number and intrinsic frequencies in particle-laden flows. AIAA J. 32, 1322–1325.
Ayranci, R., Pinguet, G., Escudié, D., Selçuk, N., Vaillon, R., André, 2007. Effect of particle polydispersity on particle concentration measurement by using laser Doppler anemometry. Exp. Therm. Fluid Sci. 31, 839–847.
Batchelor, G.K., 1971. J. Fluid Mech. 46, 813–829.
Crowe, C.T., Gore, R., Troutt, T.R., 1985. Particle dispersion by coherent structures in free shear flows. Particul. Sci. Technol. 3, 149–158.
DeSpirito, J., Wang, L.-P., 2001. Linear instability of two-way coupled particle-laden jet. Int. J. Multiphase Flow 27, 1179–1198.
Di Giancinto, M., Sabetta, F., Piva, R., 1982. Two-way coupling effects in dilute gas-particle flows. J. Fluids Eng. 104, 304–312.
Fan, J., Zhang, L., Zhao, H., Cen, K., 1990. Particle concentration and particle size measurements in a particle laden turbulent free jet. Exp. Fluids 9, 320–322.
Fan, J., Zhao, H., Cen, K., 1992. An experimental study of two-phase turbulent coaxial jets. Exp. Fluids 13, 279–287.
Fleckhaus, D., Hishida, K., Maeda, M., 1987. Effect of laden solid particles on the turbulent flow structure of a round free jet. Exp. Fluids 5, 323–333.
Geiss, S., Dreizler, A., Stojanovic, Z., Chrigui, M., Sadiki, A., Janicka, J., 2004. Investigation of turbulence modification in a non-reactive two-phse flow. Exp. Fluids 36, 344–354.
Hardalupas, Y., Horender, S., 2003. Fluctuations of particle concentration in a turbulent two-phase shear layer. Int. J. Multiphase Flow 29, 1645–1667.
Hardalupas, Y., Taylor, A.M.K.P., Whitelaw, J.H., 1989. Velocity and particle-flux characteristics of turbulent particle-laden jets. Proc. R. Soc. Lond. A 426, 31–78.
Kalt, P.A.M., Nathan, G.J., 2007. Corrections to facilitate planar imaging of particle concentration in particle-laden flows using Mie-scatting. Part 2. Diverging laser sheets. Appl. Opt. 46, 7227–7236.
Kalt, P.A.M., Birzer, C.H., Nathan, G.J., 2007. Corrections to facilitate planar imaging of particle concentration in particle-laden flows using Mie-scatting. Part 1. Collimated laser sheets. Appl. Opt. 46, 5823–5834.
Longmire, E.K., Eaton J.K., 1990. Structure and control of a particle-laden round jet, Internal Report, MD-58, Stanford University.
Longmire, E.K., Eaton, J.K., 1992. Structure of a particle-laden round jet. J. Fluid Mech. 236, 217–257.
Megalos, N.P., Smith, N.L., Zhang, D.K., 2001. The potential for low NO_X from a precessing jet burner of coal. Combust. Flame 1245, 50–64.
Nathan, G.J., 1988. The enhanced mixing burner, Ph.D. Thesis, The University of Adelaide.
Nathan, G.J., Hill, S.J., 2001. Performance assessment of the solid fuel gyro-therm burner, ash grove cement, Durkee, Oregon, Internal Interim Report.
Nathan, G.J., Hill, S.J., 2002. Full scale assessment of the influence of a precessing jet of air on the performance of pulverised coal flame in a cement kiln. In: Proceedings of the Sixth European Conference on Industrial Furnaces and Boilers (INFUB), Lisbon, Portugal, April 2–5.
Nathan, G.J., Luxton, R.E., 1992. Reduced NO_X emissions and enhanced large scale turbulence from a precessing jet burner. Proceedings of the 24th Symposium (International) on Combustion. The Combustion Institute. pp. 1399–1405s.
Nathan, G.J., Manias, C.G., 1995. The role of process and flame interaction in reducing NO_X emissions. Combust. Emission Control, 309–312.
Nathan, G.J., Hill, S.J., Luxton, R.E., 1998. An axisymmetric "fluidic" nozzle to generate jet precession. J. Fluid Mech. 370, 347–380.
Nathan, G.J., Smith, N.L., Mullinger, P.J., Smart, J.P., 2000. Performance characteristics of, and an aerodynamic scaling parameter for, a practical PF burner design employing jet excitation to promote particle clustering. In: Proceedings of the Fifth International Conference on Industrial Furnaces and Boilers.
Nathan, G.J., Mi, J., Alwahabi, Z.T., Newbold, G.J.R., Nobes, D.S., 2006. Impacts of a jet's exit flow pattern on mixing and combustion performance. Progr. Energy Combust. Sci. 32, 496–538.
Ono, Y., 1980. Microscopical estimation of burning condition and quality of clinker. In: Proceedings of the Seventh International Congress of Chemistry of Cement, vol. 2, pp. 206–211.
Parham, J.J., Nathan, G.J., Smart, J.P., Hill, S.J., Jenkins, B.G., 2000. The relationship between heat flux and NO_X emissions in gas fired rotary kilns. J. Inst. Energy 73, 25–34.
Schneier, G.M., Hooper, J.D., Musgrove, A.R., Nathan, G.J., Luxton, R.E., 1997. Velocity and reynolds stresses in a precessing jet flow. Exp. Fluids 22, 489–495.
Sheun, J.-S., Solomon, A.S.P., Zhang, Q.-F., Faeth, G.M., 1985. Structure of particle-laden jets: measurements and predictions. AIAA J. 23, 396–404.
Smart, J.P., 1992. On the effect of burner scale and coal quality on low NO_X burner performance, Ph.D. Thesis, University of London, London, England.
Smith, N.L., Megalos, N.P., Nathan, G.J., Zhang, D.K., Smart, J.P., 1998a. The role of fuel rich clusters in flame stabilisation and NO_X emissions reduction with precessing jet pf flames. Proceedings of the 27th Symposium (International) on Combustion, vol. 27. The Combustion Institute. pp. 3173–3179.
Smith, N.L., Megalos, N.P., Nathan, G.J., Zhang, D.K., Smart, J.P., 1998b. Precessing jet burners for stable and low NO_X pulverised fuel flames – preliminary results from scall-scale trials. Fuel 77, 1013–1016.
Smith, N.L., Nathan, G.J., Zhang, D.K., Nobes, D.S., 2002. The significance of particle clustering in pulverised coal flames. Proceedings of the 29th Symposium (International) on Combustion, vol. 29. The Combustion Institute. pp. 797–804.
Uchiyama, T., Fukase, A., 2006. Vortex simulation of gas-particle two-phase compound round jet. Powder Technol. 165, 83–91.
Wicker, R.B., Eaton, J.K., 1999. Effect of injected longitudinal vorticity on particle dispersion in a swirling coaxial jet. Trans. Am. Soc. Mech. Eng. 121, 766–772.
Wicker, R.B., Eaton, J.K., 2001. Structure of a swirling recirculating coaxial free jet and its effect on particle motion. Int. J. Multiphase Flow 27, 949–970.
Wong, C.Y., Lanspeary, P.V., Nathan, G.J., Kelso, R.M., O'Doherty, T., 2003. Phase-averaged velocity in a fluidic precessing jet nozzle and in its near external field. Exp. Therm. Fluid Sci. 27, 515–524.